



## Enhancing corrosion resistance of Ti<sub>2</sub>AlC MAX phase through Sn solid solution in harsh acidic environments

Jiayue Zhang<sup>a,b</sup>, Yan Zhang<sup>a</sup>, Zhenyu Wang<sup>a</sup>, Guanshui Ma<sup>a,\*</sup>, Anfeng Zhang<sup>a</sup>, Kwang-Ryeol Lee<sup>c</sup>, Aiying Wang<sup>a,\*</sup> 

<sup>a</sup> State Key Laboratory of Advanced Marine Materials, Ningbo Institute of Materials Technology and Engineering, Chinese Academy of Sciences, Zhejiang, Ningbo 315201, China

<sup>b</sup> School of Materials Science and Chemical Engineering, Ningbo University, Zhejiang, Ningbo 315211, China

<sup>c</sup> Computational Science Center, Korea Institute of Science and Technology, Seoul 136-791, Republic of Korea

### ARTICLE INFO

#### Keywords:

MAX phase coating  
Sn solid solution Ti<sub>2</sub>AlC  
Corrosion resistance  
Conductivity  
Passivation film

### ABSTRACT

When proton exchange membrane fuel cells (PEMFCs) run in the harsh acidic environment at 60–80 °C, metallic bipolar plates are prone to dissolution and corrosion, leading to increased interfacial contact resistance (ICR) and a decrease in output power energy. In this work, high-purity Ti<sub>2</sub>AlC MAX phase coatings, with and without Sn solid solution, were fabricated on 316 L stainless steel using a multiple sputtering technique followed by a subsequent heat treatment process. Effect of Sn modification on the corrosion resistance and electrical conductivity of coatings was particularly focused on under simulated PEMFCs conditions. The results indicated that the Ti<sub>2</sub>(Al, Sn)C coating significantly improved electrical conductivity and corrosion resistance compared to the pristine Ti<sub>2</sub>AlC coating. The observed phenomena in Ti<sub>2</sub>(Al, Sn)C coating could be attributed to the unique appearance of passivation layer, where three layers—TiO<sub>2</sub>, Al<sub>2</sub>O<sub>3</sub> and SnO<sub>2</sub>— were identified distinctly. One benefit was that the outermost SnO<sub>2</sub>, resulting from the oxidation of Sn, partially inhibited the penetration of corrosive media. This enhancement improved the protective efficiency of the subsequent Al<sub>2</sub>O<sub>3</sub> layer, which has a higher density than that of TiO<sub>2</sub> layer. On the other hand, the microstructure evolution of the passivation film was also well consistent with the capability of atomic diffusion, as indicated by the atomic vacancy formation energy and the migration energy by density functional theory simulation. As a result, the unusual layered oxides in the Ti<sub>2</sub>(Al, Sn)C coating enhanced the corrosion resistance and ICR value of the coatings compared to the pristine Ti<sub>2</sub>AlC coating.

### 1. Introduction

Proton exchange membrane fuel cells (PEMFCs) are representative candidates for hydrogen energy. They offer advantages such as high specific energy, rapid low-temperature startup, and stable operation. These features make them promising for various applications, including power generation, aerospace, marine, and distributed small-scale power stations[1]. As the core components carrying battery current and separating reaction gases in PEMFCs[2], metallic bipolar plates account for approximately 40 % of the stack cost, 80 % of the weight, and 75 % of the volume. However, during the operation parameters of PEMFCs systems, the bipolar plates are subjected to high temperature (60–80 °C) and harsh acidity (pH 2–3) with HF+H<sub>2</sub>SO<sub>4</sub> solution. This environment accelerates the dissolution and severe corrosion of the plate materials.

As a result, the interfacial contact resistance (ICR) increases, and the electrodes are poisoned, leading to a reduction in output efficiency and service lifetime of fuel cells [3].

Surface coating technology is an advanced process that enhances materials performance by applying specialized functional layers onto substrate surfaces. This technique can form protective coatings at micron or nanometer scales, endowing materials with new physical, chemical, or mechanical properties. Common coating methods include Physical Vapor Deposition (PVD), Chemical Vapor Deposition (CVD), thermal spraying, and electroplating. Depending on requirements, these coatings can provide various functionalities such as wear resistance, corrosion protection, thermal insulation, electrical conductivity, or esthetic improvement. As a vital component of modern materials engineering, this technology finds widespread applications across

\* Corresponding authors.

E-mail addresses: [maguanshui@nimte.ac.cn](mailto:maguanshui@nimte.ac.cn) (G. Ma), [aywang@nimte.ac.cn](mailto:aywang@nimte.ac.cn) (A. Wang).

<https://doi.org/10.1016/j.corsci.2025.113073>

Received 13 April 2025; Received in revised form 13 May 2025; Accepted 28 May 2025

Available online 29 May 2025

0010-938X/© 2025 Elsevier Ltd. All rights are reserved, including those for text and data mining, AI training, and similar technologies.

mechanical manufacturing, electronic devices, aerospace, medical equipment and other industrial fields[4–7]. In recent years, surface coating technology has emerged as a strong strategy to enhance the conductivity and corrosion resistance of metallic bipolar plates without deteriorating their intrinsic properties. Various attempts have been made to develop conductive and anticorrosion coatings, including noble metal coatings[8], metallic carbide coatings[9], conductive polymer composite coatings[10], amorphous carbon coatings[11], and  $M_{n+1}AX_n$  (MAX) phase coatings[12–14]. Among them, MAX phase coatings are particularly attractive due to their nanolaminate hexagonal structure. In this structure, the MX and A layers stack alternately along the c-axis, consisting of strong M-X bonds and relatively weak M-A bonds [15–20]. This unique structure enables MAX phase coating a superior combination of metallic and ceramic properties, such as high electrical, corrosion resistance, thermal conductivity, high-temperature oxidation resistance and high strength. Particularly,  $Ti_2AlC$  MAX phase exhibits a high electrical conductivity of  $4.42 \times 10^6 \Omega^{-1} m^{-1}$  at room temperature, which is over 2 times that of pure Ti[21]. Additionally,  $Ti_2AlC$  demonstrates good stability in both alkaline and acidic solutions[22]. These performances make  $Ti_2AlC$  MAX phase coatings promising candidate for improving corrosion resistance and conductivity of metallic bipolar plates.

Basically, the excellent corrosion resistance of MAX phase coatings can be attributed to the formation of a self-adaptive passivation film during surface oxidation process in PEMFCs. Barsoum et al.[23] investigated the electrochemical behavior of  $Ti_3SiC_2$  in strong acidic and alkaline environments. They found the high anticorrosion arose from the generated  $SiO_2$  passivation layer during oxidation. Similarly, Li et al. [24] examined the corrosion resistance of  $Ti_3AlC_2$  in  $H_2SO_4$  and NaOH solutions. They discovered found that only a metastable  $TiO_{2-x}$  passivation film formed in  $H_2SO_4$  solution. In contrast, a dense and stable  $TiO_2$  passivation film was generated in NaOH, providing better resistance than that in  $H_2SO_4$ . Lu et al.[25] conducted a 24 h potentiostatic polarization test on a  $Ti_3AlC_2$  MAX phase coating under simulated PEMFCs condition (PH 3  $H_2SO_4$  + 2 ppm F, 70 °C). The results showed that the coating maintained a low corrosion current density. However, the emergence of the semiconductor passivation film increased the ICR value to  $11.85 m\Omega \cdot cm^2$ , which was 3.2 times higher than before corrosion test. Recently, we prepared  $Cr_2AlC$  MAX phase coatings and investigated their corrosion stability and electrical conductivity under accelerated PEMFCs conditions[26,27]. After 12 h of potentiostatic polarization, it was found that the increase of ICR value was closely related to the formed passivation layer. In this case, manipulating the passive layers could be a promising approach to enhance the corrosion resistance and reduce post-corrosion ICR for MAX phase materials.

It is possible to modify the passivation film after corrosion by alloying MAX phase with solid-solutioning elements, without the formation of a second phase[28–30]. For example, Barsoum et al.[31] reported that the corrosion current density of  $(Ti, Nb)_2AlC$  was reduced by an order of magnitude compared to that of pristine  $Ti_2AlC$  in 1 M  $H_2SO_4$  solution. This reduction is due to the presence of a stable passivation film. Increasing the Si content in  $Ti_3(Al_{1-x}Si_x)C_2$  MAX phase led to a higher  $SiO_2$  content in the passivation film when exposed to 3.5 wt% NaCl solution[31,32]. Consequently, the growth of passivation film favored a decrease in carrier concentration and an increase in charge transfer resistance. This change subsequently reduces the corrosion current density and improves corrosion performance. Of cause, considering the advantages of the Hume-Rothery rule, Sn could be infinitely soluble in the A-site of the  $Ti_2AlC$  system. Recently, Bei et al.[33] prepared the  $Ti_2Al_{(1-x)}Sn_xC$  MAX phases with x ranging from 0 to 1. The results showed the formation of  $SnO_2$  was preferred over  $TiO_2$  and  $Al_2O_3$  during the oxidation process. This preference enhances oxidation resistance. Moreover,  $SnO_2$  is a stable n-type semiconductor in acidic solutions and an excellent transparent conductive material. Its conductivity ( $10^{-4} \Omega^{-1} cm^{-1}$ ) is  $10^6$  times higher than that of  $TiO_2$ [34]. Therefore, Sn substitution in the A-site is expected to further improve

the corrosion resistance and reduce the ICR for  $Ti_2AlC$  MAX phase coatings after extreme corrosion[35–38].

However, the electrochemical corrosion behavior and conductive performance of Sn-substituted MAX phase materials have not been extensively studied in harsh acidic solution like  $HF+H_2SO_4$  for PEMFCs systems. In addition, dependence of electrochemical properties on evolution of passive layer on Sn solid-solution has not been clearly understood yet. In this work, we fabricated the  $Ti_2AlC$  and  $Ti_2(Al, Sn)C$  MAX phase coatings on stainless steel 316 L (SS316L) substrates using a hybrid high-power pulsed magnetron sputtering (HiPIMS), followed by annealing treatment. In particular, the corrosion resistance and electrical conductivity were focused in terms of Sn alloying in MAX phase matrix under the harsh 0.5 M  $H_2SO_4$  + 5 mg/L HF solution. The results not only provide the in-depth mechanism for the electrochemical corrosion of  $Ti_2(Al, Sn)C$  MAX phase coatings, but also offer a promising strategy of advanced coating to modify the working performance of metallic plates used for PEMFCs with high performance and long lifetime.

## 2. Experimental details

### 2.1. Coatings preparation

The Ti-Al-C and Ti-Al-Sn-C coatings were deposited on SS316L substrates by a hybrid HiPIMS/direct current magnetron sputtering (DCMS) technique with a multi-target sources. The nominal composition of the SS316L (wt%) was: C, 0.014; P 0.023; S, 0.001; Cr, 22.39; Ni, 5.68; N, 0.17; Mo, 3.13; Si, 0.39; Mn, 1.38, and balance Fe. All the SS316L substrates with size of  $\Phi 14 mm \times 3 mm$  (thickness) were ground with No. 800–5000 grit by SiC abrasive papers, and polished by No. 5 diamond paste polisher. To remove residual surface contaminants before putting them into the chamber, the SS316L substrates were ultrasonically cleaned by acetone and alcohol for 15 min, and dried using high-purity  $N_2$ . Three various targets including Ti target, Al or AlSn alloy target (Al:Sn = 90:10 at%) and graphite target was used for the coating deposition. All the target materials had a purity of 99.9 %, and the targets size were  $\Phi 50.8 mm \times 5 mm$ . The distance between the substrates and the targets was about 12 mm. Before deposition, the chamber was evacuated to a base pressure of  $3 \times 10^{-5}$  Pa, and the sample holder was heated to 120 °C. Then the substrates were etched by  $Ar^+$  ions for 30 min using a pulsed bias of  $-600 V$  to remove contaminants and oxides from the substrate surface. During deposition, the Ti target was operated by a HiPIMS power supply, while the AlSn/Al target and the C target were controlled by DCMS modes in view of the low ionization rate of C and low melting point of Sn. Noted that, a TiC transition layer with a thickness of approximately 0.2  $\mu m$  was deposited on the substrate in order to enhance the adhesion strength between coating and substrate. Subsequently, a Ti-Al-C or Ti-Al-Sn-C coating with a 2  $\mu m$ -thickness was prepared by co-sputtering technique on top of the TiC-transition layer. The schematic diagrams of the multi-target magnetron sputtering system was shown in Fig. 1. The parameters for the deposition process were set as follows: argon pressure at 0.7 Pa, pulsed bias voltage of  $-100 V$  for substrate, Ti target power at 100 W (HiPIMS) with a duty cycle of 5 %, Al target power of 50 W (DCMS) and C target power at 33–45 W (DCMS). It was noted that, for the Ti-Al-C coating, the process was similar to Ti-Al-Sn-C, except that the AlSn target was replaced with an Al target applying with a reduced power to 50 W. During coating deposition, all the substrate temperature was 120 °C. Finally, both the as-deposited Ti-Al-Sn-C and Ti-Al-C coatings were annealed using a rapid thermal furnace at a vacuum level of  $3 \times 10^{-4}$  Pa, where the samples were heated to a temperature of 750 °C at a rate of 10 °C/min with holding for 90 min. Afterward, the samples were allowed to cool naturally back to room temperature.

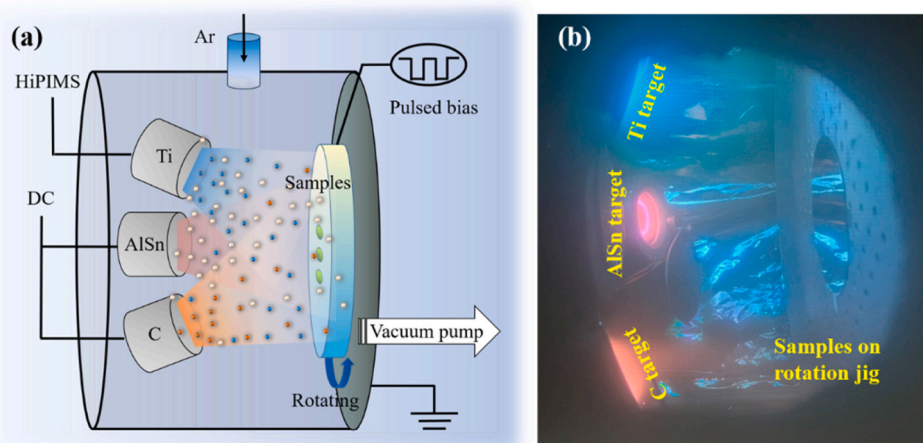


Fig. 1. (a) Schematic diagrams of the multi-target magnetron sputtering system. (b) Photograph of discharge plasma during coating deposition.

## 2.2. Characterization methods

The surface morphology and chemical composition of the annealed coatings were characterized using a scanning electron microscope (SEM, FEI Quanta FEG 250) equipped with an energy dispersive X-ray spectrometer (EDS). The phase composition and crystal structure information of the coatings were analyzed using X-ray diffraction (XRD) with a Bruker D8 Advance X-ray diffractometer. This instrument utilizes Cu K $\alpha$  ( $\lambda = 1.54056 \text{ \AA}$ ) radiation, operating at a voltage of 40 kV and a current of 40 mA, with a grazing incidence angle of  $2^\circ$ . The scanning range was from  $10^\circ$  to  $90^\circ$ , with a step size of  $0.02^\circ$  per step. The XRD results were compared with standard PDF cards using Jade 6.0 software to confirm the phases present in the coatings. X-ray photoelectron spectroscopy (XPS) was performed using an AXIS SUPRA system to investigate the elemental composition and chemical bonding states of the coating surfaces. The X-ray source of this XPS instrument is a monochromated Al K $\alpha$  radiation with a photon energy of 1486.6 eV. Data collection and analysis were conducted using the instrument's built-in ESCAPE software, while high-resolution spectra for specific elements were processed and analyzed using CasaXPS software. Transmission electron microscopy (TEM) and high-resolution electron microscopy (HRTEM) analyses were performed on a TALOS F200 field emission transmission electron microscope operating at 200 keV. Scanning transmission electron microscopy (STEM) and EDS analysis were conducted on the Talos F200 equipped with a high-angle annular dark-field (HAADF) detector.

## 2.3. Electrochemical and conductivity measurements

All the corrosion resistance tests were carried out in 0.5 M H $_2$ SO $_4$  + 5 mg/L HF solution at 80 °C by Gamry electrochemical workstation, during which the work area was normalized to 1 cm $^2$ . The as-prepared samples were used as the working electrode, with a saturated calomel electrode (SCE) as the reference electrode and a platinum plate as the counter electrode. Potentiodynamic polarization curves of the coatings were recorded in the potential range of  $-0.6 \text{ V}$  to  $0.8 \text{ V}$  (vs. SCE) at a scan rate of  $0.5 \text{ mV s}^{-1}$ . Additionally, to evaluate the corrosion stability of the coatings, potentiostatic measurements were performed at a constant potential of  $0.6 \text{ V}$  (vs. SCE) for 24 h. The methods for ICR evaluation and electrochemical measurements were the same as in our previous work[27]. Carbon paper (Toray TGP-H-60) was sandwiched between the test samples and two gold-plated copper plates, and a certain compressive force was applied using a microcomputer-controlled mechanical testing machine (CMT5150, US). The total resistance of the carbon paper under different compaction pressures was measured using a low-DC-resistance tester (JK2511B).

## 2.4. Atomic-scale calculations

The first principles calculation in this work was performed using the Cambridge Sequential Total Energy Package (CASTEP), that employed the density functional theory (DFT) based on the plane-wave pseudo-potential method[39]. The generalized gradient approximation constructed by Perdew-Burke-Ernzerhof (GGA-PBE) was applied for the exchange correlation energy function[40]. The Ti $_2$ AlC MAX phases are crystallized in hexagonal structure with the space group  $P6_3/mmc$ . There are 8 atoms in the unit cell of which 4Ti, 2Al and 2 C atoms are contributed to the total 8 atoms, and the position of carbon atoms is 2a, Ti atoms is 4 f and Al atoms is 2c Wyckoff positions[41]. And then a  $2 \times 2 \times 1$  supercell containing 32 atoms was adopted to simulate the defect formation and migration process. Afterwards, a Al atom in the Ti $_2$ AlC supercell were substituted by Sn atom, and then, the structure of Ti $_2$ (Al,Sn)C are formed. The relevant model diagrams are presented in the calculation results section. Specifically, the defect formation process was evaluated by calculating the formation energy. The self-diffusion barrier for each atom along the basal plane in the Ti $_2$ (Al, Sn)C phase was assessed by identifying the transition state that connects two defective configurations. This was conducted by the linear synchronous transit (LST) or quadratic synchronous transit (QST) methods along with conjugate gradient refinements[42].

## 3. Result and discussion

### 3.1. Characterization of Ti $_2$ AlC and Ti $_2$ (Al, Sn)C coatings

Fig. 2 shows the X-ray diffraction (XRD) patterns of the Ti $_2$ AlC and Ti $_2$ (Al, Sn)C coatings. According to the standard PDF#29-0025 card [43], it was apparent that the coatings exhibited a high-purity Ti $_2$ AlC crystalline phase beyond the substrate features [44]. Different with Ti $_2$ (Al, Sn)C coating, there was a small amount of TiC impurity identified in Ti $_2$ AlC case. From the enlarged X-ray diffractograms in the  $2\theta$  between  $38^\circ$  and  $44^\circ$  (Fig. 2b), there was no peak shift for the SS 316 L substrate. However, the peaks between  $38^\circ$  and  $41^\circ$  exhibited a downward shift for the crystalline planes of the MAX phases. This peak downshift might be attributed to the larger atomic radius of the Sn substitution compared to that of Al atom (atomic radius: Sn=0.145 nm, Al=0.125 nm). This difference caused an expansion of the MAX phase lattice parameters [43]. As shown in Fig. 3a-b, no distinct changes were observed in the surface morphology for Ti $_2$ AlC and Ti $_2$ (Al, Sn)C coatings. All the coatings exhibited a dense and uniform microstructure without visible pinholes or crack defects, regardless of the Sn solid solution. Therefore, it could be concluded that Sn has been successfully

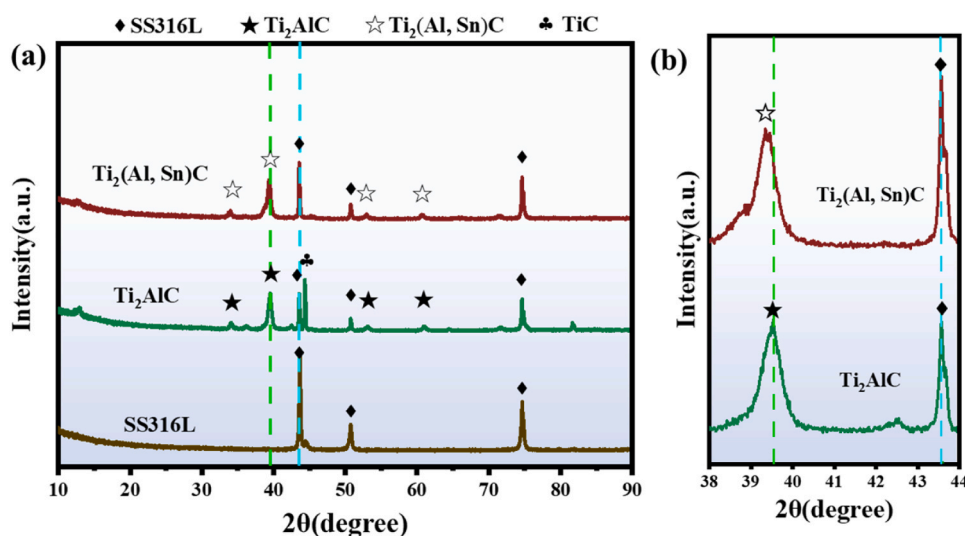


Fig. 2. (a) XRD patterns. (b) Local enlarged images over  $2\theta$  range  $38^\circ$  to  $44^\circ$ .

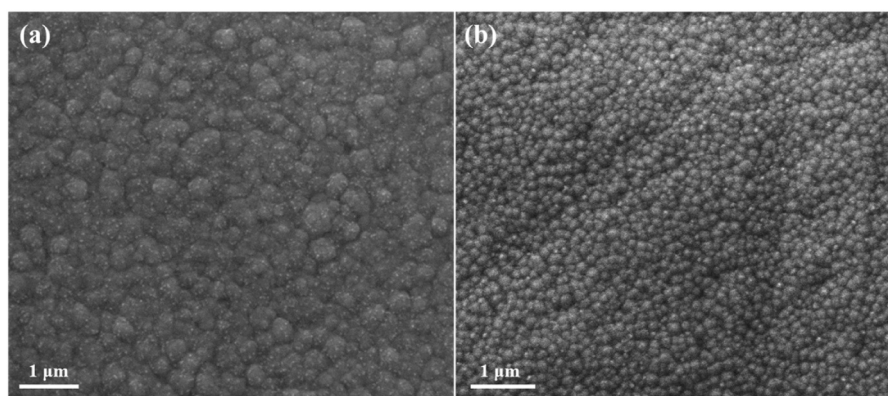


Fig. 3. (a) Surface morphologies of  $Ti_2AlC$  coating (b)  $Ti_2(Al, Sn)C$  coating.

solid-solved into the  $Ti_2AlC$  matrix, forming a high-purity  $Ti_2(Al, Sn)C$  MAX phase coating in this work.

To further identify the chemical composition and atomic bonding characteristics of the coatings, XPS measurements were carried out and the results were shown in Fig. 4. For the Ti 2p spectra (Fig. 4a), no significant differences were observed. The spectra could be deconvoluted into four peaks at binding energies of 454.8 eV, 458.8 eV, 460.9 eV, 464.9 eV for  $Ti_2AlC$  coating. The  $Ti_2(Al, Sn)C$  coating showed peaks at 455.1 eV, 458.4 eV, 461.2 eV, 464.5 eV. The peaks at 454.8 eV and 460.9 eV ( $Ti_2AlC$ ) arise from the Ti  $2p^{3/2}$  and Ti  $2p^{1/2}$ , which are related to the  $Ti_2AlC$  phase [45], while the other peaks were associated with Ti-O bonds [46]. Once the Sn was evolved in MAX phase matrix, the peaks shifted upwards to binding energies at 455.1 eV and 461.2 eV. This shift indicates a change in the chemical characteristics due to the formation of new Sn-related bonds. On the other hand, the Al 2p spectra (Fig. 4b) were associated with Al-Ti and Al-O bonds [47,48]. A key observation is that the Al-O bond is much stronger than the Al-Ti bond. This suggests possible oxidation of the coating surface during the annealing process [49].

Compared to the expected lack of Sn feature in the  $Ti_2AlC$  coating, the  $Ti_2(Al, Sn)C$  coating clearly demonstrated Sn 3d peaks at 484.5 eV, 488.1 eV, 492.9 eV, and 496.5 eV (Fig. 4c). The peaks at 484.5 eV and 492.9 eV correspond to Sn  $3d^{5/2}$  and Sn  $3d^{3/2}$  [50,51], while the peaks at 488.1 eV and 496.5 eV were attributed to Sn-O bonds [52]. After deconvoluting the C 1s spectra (Fig. 4d), the  $Ti_2AlC$  coating revealed three peaks at 282.1 eV, 285.7 eV, 289.7 eV. The  $Ti_2(Al, Sn)C$  coating

showed peaks at 282.0 eV, 286.6 eV, 289.5 eV. Meanwhile, the peaks at 282.1 eV and 282.0 eV were identified as Ti-C bonds in both coatings [47,48,53]. Based on the comprehensive XPS analysis, the Sn solid solution in high-purity  $Ti_2AlC$  coating is consistent with the XRD results.

Advanced atom-resolution high-angle annular dark-field (HAADF) imaging technique was employed to have a more in-depth analysis of the microstructure of the solid solution coating. The results are depicted in Fig. 5a-b. The unique nanolayered structure of MAX phase is clearly visible, composed mainly of alternately stacked two layers of Ti-C plates and one layer of interleaved Al(Sn) atoms, with the absence of C atoms due to the weak diffraction ability in the STEM image. Regrettably, the arrangement of Sn atoms in the  $Ti_2AlC$  Al position was not clearly observed, attributed to the small nanocrystalline grain size ( $\sim 10$  nm) of the prepared coating. However, there's no doubt that, the atomic-level EDS results (Fig. 5c-h) clearly indicate the presence of Sn elements, with a uniform distribution. Furthermore, combined with the XRD analysis results, there are no other impurity phases containing Sn in the prepared coating. Thus, it can be conclusively stated that Sn atoms are certainly present in the form of solid solution in the  $Ti_2AlC$  coating.

### 3.2. Electrochemical properties

As shown in Fig. 6a-b, electrochemical impedance spectroscopy (EIS) was performed on two coatings under harsh acidic solution ( $0.5 \text{ mol H}_2\text{SO}_4 + 5 \text{ mg/L HF}$ ,  $80^\circ \text{C}$ ). In the Nyquist plot (Fig. 6a), the size of the capacitive arc is related to the protectiveness of the passive

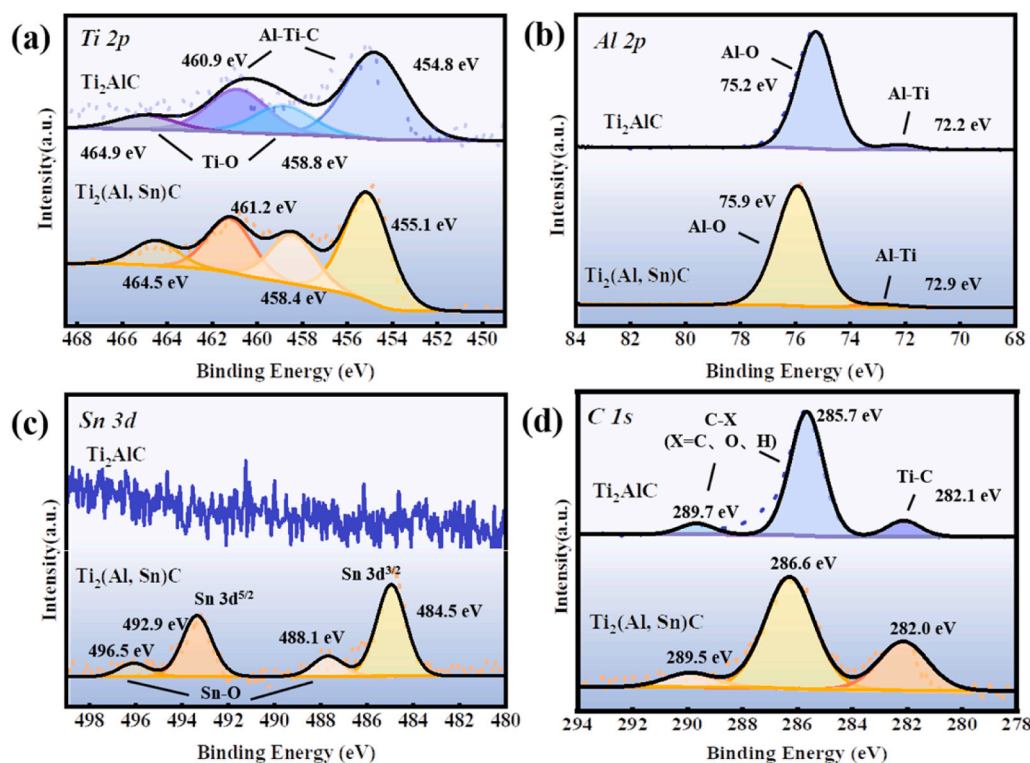


Fig. 4. XPS spectra of (a) Ti 2p, (b) Al 2p, (c) Sn 3d and (d) C 1s for the Ti<sub>2</sub>AlC and Ti<sub>2</sub>(Al, Sn)C coatings.

film formed on the coating. A larger capacitive arc radius generally indicates a higher resistance of passive film, indicating stronger charge transfer resistance and better corrosion resistance of the electrode system[54]. Therefore, since the capacitive arc radius of the Ti<sub>2</sub>(Al, Sn)C coating is significantly larger than that of the Ti<sub>2</sub>AlC coating, it could be concluded that the Ti<sub>2</sub>(Al, Sn)C coating displays better electrochemical corrosion resistance. Similarly, the corresponding Bode plot (Fig. 6b) confirmed that the higher  $|Z|$  values and a wider range ( $10^{-2}$ ~ $10^2$  Hz) of phase angles were observed for Ti<sub>2</sub>(Al, Sn)C coating compared to those of Ti<sub>2</sub>AlC coating. The EIS data could be further fitted by an equivalent circuit model. In the equivalent circuit,  $R_s$  generally represents the solution resistance. It is affected by the electrolyte concentration and the electrode area. In our experiments, differences in  $R_s$  values may arise from small changes in the state of the electrode surface or experimental conditions, despite using the same solution.  $R_1$  is the passive film resistance, while  $R_{ct}$  is the charge transfer resistance at the coating/substrate interface. The difference in  $R_{ct}$  between Ti<sub>2</sub>(Al, Sn)C and Ti<sub>2</sub>AlC may relate to the formation process and surface properties of the film. Due to the dispersive effects caused by the rough surface of the coated electrode, a constant phase element (CPE) was used instead of an ideal capacitor[55].  $CPE_1$  represents the passive film capacitance, and  $CPE_2$  corresponds to the double-layer capacitance at the coating/solution and substrate/solution interfaces. Table 1 illustrates the fitting results of EIS spectra. The chi-square ( $\chi^2$ ) values were all in the range of  $10^{-4}$ , indicating that the equivalent circuit model accurately represented the electrochemical behavior of the coatings in the employed solution. In general, the resistance  $R_1$  is a direct parameter to characterize the barrier effect and protective performance of the coating against the corrosive solution. Higher  $R_1$  values indicate stronger protection of the substrate[56,57]. Based on the Table 1, the  $R_1$  value of the Ti<sub>2</sub>(Al, Sn)C coating is about  $83.81 \Omega \cdot \text{cm}^{-2}$ , which is much higher than the Ti<sub>2</sub>AlC coating ( $52.56 \Omega \cdot \text{cm}^{-2}$ ), indicating the better protective capability of the Ti<sub>2</sub>(Al, Sn)C coating. The higher  $R_{ct}$  value of Ti<sub>2</sub>(Al, Sn)C indicates that better charge transfer resistance and corrosion resistance in an electrochemical environment[58–60].

Fig. 6c-e shows the polarization curves of the two coatings in the solution containing 0.5 mol H<sub>2</sub>SO<sub>4</sub> + 5 mg/L HF at 80 °C. The relevant parameters obtained from the Tafel fitting from the potentiodynamic polarization curves are listed in Table 2. For both coatings, the  $\beta_a$  values were larger than the corresponding  $-\beta_c$  values, indicating anodic control for corrosion[61]. Meanwhile, as shown in Fig. 6c, distinct passivation behavior was observed for both coatings, with the current density slowly decreasing or remaining constant. This indicates that corrosion of the samples was dominated by the formation of passive oxide film. The corrosion current density ( $I_{corr}$ ) is proportional to the corrosion rate and it is an important parameter for evaluating the corrosion resistance of materials[62]. Compared to the Ti<sub>2</sub>AlC coating ( $I_{corr} = 1.35 \times 10^{-5}$  A/cm<sup>2</sup>), the current density for the Ti<sub>2</sub>(Al, Sn)C coating was reduced about two orders of magnitude ( $I_{corr} = 3.36 \times 10^{-7}$  A/cm<sup>2</sup>). Furthermore, 24-hour potentiostatic polarization was conducted to test the durability of the coatings. As shown in Fig. 6d, the high reactivity of Ti was easily dissolved in such acidic solution at 80 °C, leading to an increase in current density[63]. However, once the oxide layer emerged, corrosion was mitigated and the current density reached a stable situation. In this case, the stabilized current densities were  $8.19 \times 10^{-6}$  A/cm<sup>2</sup> for Ti<sub>2</sub>AlC coating and  $9.62 \times 10^{-7}$  A/cm<sup>2</sup> for Ti<sub>2</sub>(Al, Sn)C coating (Fig. 6e). This further evidences the superior corrosion resistance observed in Ti<sub>2</sub>(Al, Sn)C coating. According to the U.S. Department of Energy DOE standards, coatings for bipolar plates are required to have a corrosion current density of less than  $1.00 \times 10^{-6}$  A/cm<sup>2</sup>. Ti<sub>2</sub>(Al, Sn)C coatings meet the requirements.

As another key factor for MAX phase coatings used for metallic bipolar plates under stimulated PEMFCs operation, the corrosion behavior of MAX phase coating also closely affects the ICR for output efficiency. Fig. 6f shows the comparative ICR values for the Ti<sub>2</sub>AlC and Ti<sub>2</sub>(Al, Sn)C coatings before and after constant potential polarization testing. For the pristine Ti<sub>2</sub>AlC coating, the ICR values were increased from  $13 \text{ m}\Omega \cdot \text{cm}^2$  to  $45 \text{ m}\Omega \cdot \text{cm}^2$  after corrosion test. However, the corrosion test only resulted in quite small changes in ICR, from  $9 \text{ m}\Omega \cdot \text{cm}^2$  to  $9.4 \text{ m}\Omega \cdot \text{cm}^2$  for the Ti<sub>2</sub>(Al, Sn)C coating. Since the MAX phases typically exhibit high

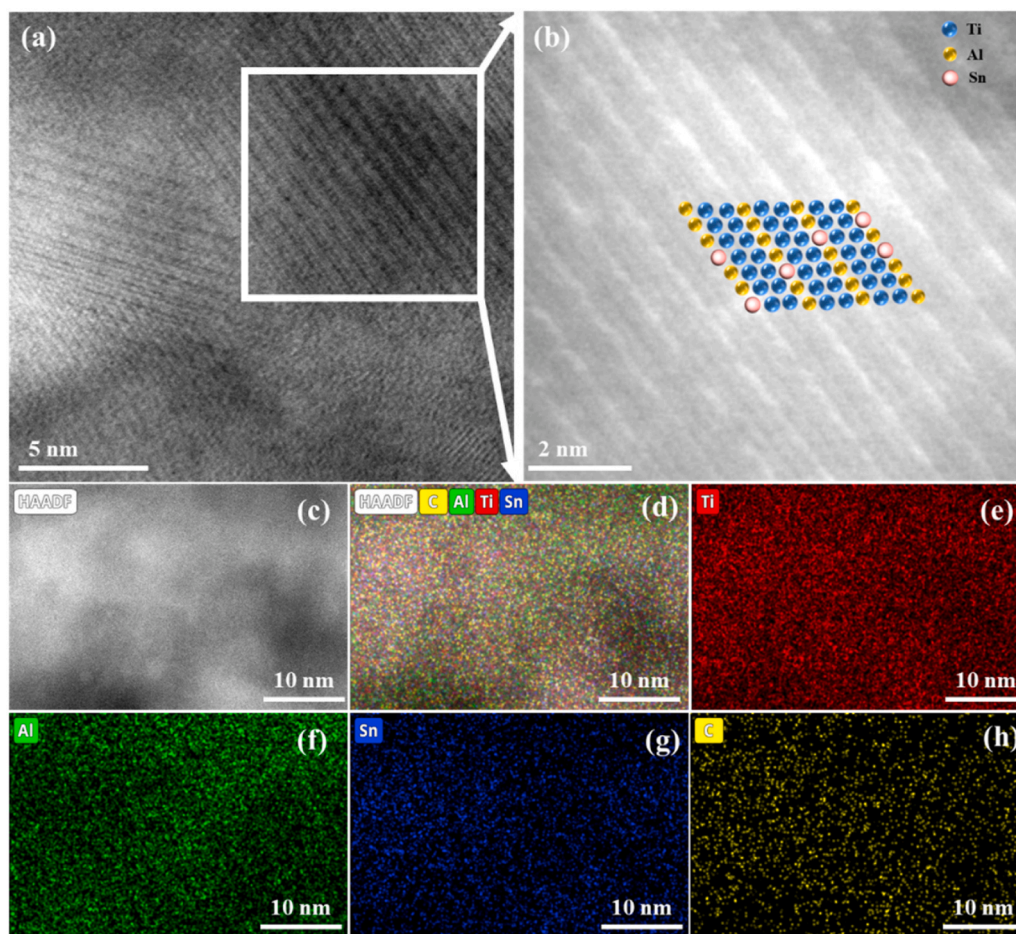


Fig. 5. (a) Atom-resolved HAADF images. (b) Enlarged image of the labeled area in (a). (c-h) Atom-resolved EDS mapping images and deduced elemental concentrations.

conductivity due to the high electron density at the Fermi level[27], the current increase in ICR for  $Ti_2AlC$  coating after corrosion could be attributed to the formed passivation film and corrosion products. Nevertheless, in case of the  $Ti_2(Al, Sn)C$  coating, the solid solution of Sn benefited the stabilization of electrical conductivity due to the well-conductive  $SnO_2$  layer formed after corrosion.

### 3.3. Passive film characteristics

To further clarify the structural evolution of passivation films for the  $Ti_2AlC$  and  $Ti_2(Al, Sn)C$  coatings, we employed focused ion beam technology to extract cross-sections of the samples after 24 h of potentiostatic polarization. To avoid damaging the oxide layers, a protective carbon layer was deposited on the sample surface before the cutting process. Fig. 7 shows the STEM-HAADF image of the  $Ti_2AlC$  coating and the corresponding elemental distribution. Clearly, the presence of Al was very low at the surface of the passivation film, while the dominant region was predominantly composed of Ti and O within passivation layer. Specifically, the contents of Ti, Al, C, O were about 32.02 at%, 0.42 at%, 1.33 at%, 61.03 at% in Region 1, respectively, while these element composition was changed to 45.65 at%, 11.94 at%, 12.93 at%, 29.48 at% in Region 2. Based on such variations, the passivation layer could be divided into two sub-regions. In Region 1, the oxide layer only demonstrated trace amounts of Al and C atoms. The dominant elements originated from Ti and O in a ratio close to 1:2, suggesting the oxides could be assigned to  $TiO_2$  phases. In Region 2, both the Al and C contents gradually increased, along with a simultaneous reduction in Ti and O contents, indicating incomplete oxidation compared to that in region 1.

Fig. 8a-f shows detailed TEM cross-section images of the passivation film produced in the  $Ti_2AlC$  coating. According to the bright-field images of region 1 (Fig. 8d) and region 2 (Fig. 8a), the key observation was that the coating was continuous and dense. Meanwhile, the incompletely oxidized layer in region 2 indicated the more uniform distribution of equiaxed crystal grains compared to those in the fully oxide layer identified in region 1. In addition, as shown in Fig. 8b, the HRTEM image corresponding to the red marks in Fig. 8a showed the coexistence of amorphous structure and nanocrystalline phases. The nanolaminate characteristic is typical of MAX phase coatings. Moreover, the interplanar spacing determined from Fourier transform was 0.63 nm, which corresponds to the (002) plane of  $Ti_2AlC$ . Additionally, the SAED pattern in Fig. 8c confirmed the other (103), (002), and (100) diffraction rings of typical  $Ti_2AlC$ . For the fully oxide layer, the enlarged HRTEM image of the red-marked area in Fig. 8d for region 1, as shown in Fig. 8e, revealed a similar amorphous and nanocrystalline structure to that in region 2. This structure was accompanied by the halo diffraction rings of SAED pattern (Fig. 8f). Noting that the interplanar spacing of localized grains was 0.24 nm, corresponding well to the (103) plane of  $TiO_2$  (PDF#21-1272). In this regard, it could be said that the oxide layer formed in  $Ti_2AlC$  coating mainly contained  $TiO_2$  phases.

Fig. 9 shows the related TEM characterizations for the  $Ti_2(Al, Sn)C$  coating along with the corresponding elemental distributions. The image presents, from top to bottom, the  $Ti_2(Al, Sn)C$  coating, the passivation film and the deposited carbon protective layer. Based on the compositional distribution, distinct enrichment zones of different elements can be observed in the passivation film. The outermost layer of the passivation film is a thin Sn-rich layer (6.35 at%), followed by an Al-

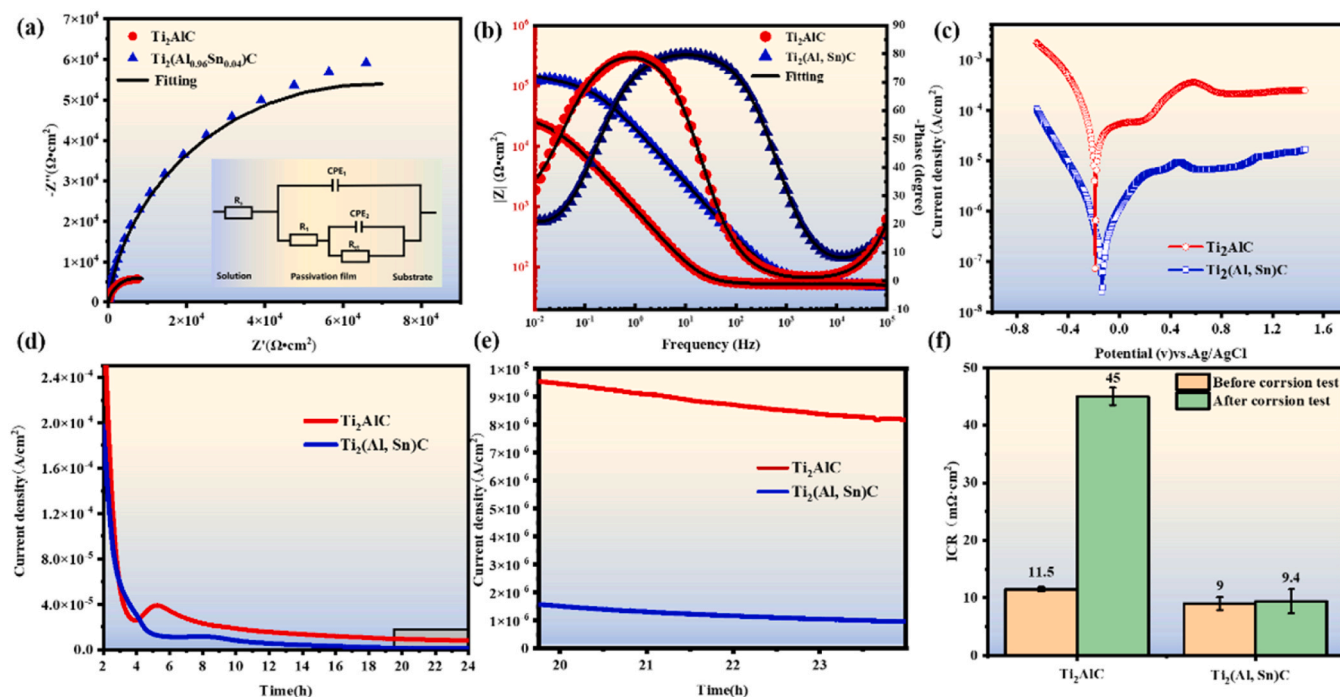


Fig. 6. EIS of  $\text{Ti}_2\text{AlC}$  and  $\text{Ti}_2(\text{Al, Sn})\text{C}$  coatings in 0.5 mol  $\text{H}_2\text{SO}_4$  + 5 mg/L HF, 80 °C: (a) Nyquist plots. (b) Bode plots. The inset in (a) is the equivalent electrical circuit used to fit the impedance spectra. (c) Potentiodynamic polarization curves of  $\text{Ti}_2\text{AlC}$  and  $\text{Ti}_2(\text{Al, Sn})\text{C}$  coatings in 0.5 mol  $\text{H}_2\text{SO}_4$  + 5 mg/L HF, 80 °C and (d) potentiostatic test curves for 24 h. (e) Local enlarged images in (d). (f) The ICR values of the samples before and after 24 h potentiostatic tests.

Table 1

Fitting results of EIS spectra for  $\text{Ti}_2\text{AlC}$  and  $\text{Ti}_2(\text{Al, Sn})\text{C}$  coatings in 0.5 mol  $\text{H}_2\text{SO}_4$  + 5 mg/L HF, 80 °C.

Simple	$R_s$ ( $\Omega \text{ cm}^{-2}$ )	CPE <sub>1</sub>		$R_1$ ( $\Omega \text{ cm}^{-2}$ )	CPE <sub>2</sub>		$R_{ct}$ ( $\Omega \text{ cm}^{-2}$ )	$\chi^2$ ( $10^{-4}$ )
		$Q_1$ ( $\text{F cm}^{-2}$ )	n		$Q_2$ ( $\text{F cm}^{-2}$ )	n		
$\text{Ti}_2\text{AlC}$	0.01	$1.41 \times 10^{-8}$	0.80	52.56	$1.98 \times 10^{-4}$	0.93	$2.24 \times 10^4$	6.33
$\text{Ti}_2(\text{Al, Sn})\text{C}$	0.02	$6.56 \times 10^{-9}$	0.99	83.81	$1.99 \times 10^{-4}$	0.94	$3.37 \times 10^5$	1.68

Table 2

Electrochemical parameters extracted from potentiodynamic polarization curves of  $\text{Ti}_2\text{AlC}$  and  $\text{Ti}_2(\text{Al, Sn})\text{C}$  coatings in 0.5 mol  $\text{H}_2\text{SO}_4$  + 5 mg/L HF, 80 °C.

Simple	$E_{corr}$ (V)	$I_{corr}$ ( $\text{A}/\text{cm}^2$ )	$\beta_a$ ( $\text{mV dec}^{-1}$ )	$-\beta_c$ ( $\text{mV dec}^{-1}$ )
$\text{Ti}_2\text{AlC}$	-0.279	$1.35 \times 10^{-5}$	744.6	167.9
$\text{Ti}_2(\text{Al, Sn})\text{C}$	-0.134	$3.36 \times 10^{-7}$	251.5	176.0

rich layer (23.38 at%), and the innermost layer consists of a thicker Ti-rich layer (27.51 at%). Different elemental enrichment zones have been delineated and marked as regions 1, 2, and 3 in the Fig. 9a. Table 3 provides the elemental composition for the red-highlighted areas in the STEM-HAADF image of Fig. 9a, corresponding to regions 1, 2, and 3.

Fig. 9b-j presents the TEM results of the cross-sections of the passivation film for regions 1, 2, and 3. The SAED patterns in Fig. 9d, g, j for regions 1 and 2, which are the Ti-rich and Al-rich layers, respectively, show diffuse and broadened wide-angle diffraction rings. Distinct diffraction rings corresponding to the  $\text{Ti}_2(\text{Al, Sn})\text{C}$  (103) plane were also measured. This suggests that there is a small amount of  $\text{Ti}_2(\text{Al, Sn})\text{C}$  MAX phase present in these two layers. Fourier transforms of the white-marked regions in Fig. 9c, f reveal interplanar spacings of 0.23 nm and 0.56 nm. These spacings correspond to the (112) plane of  $\text{TiO}_2$  and the (004) plane of  $\text{Al}_2\text{O}_3$ , respectively. Thus, while there is a small amount of  $\text{Ti}_2(\text{Al, Sn})\text{C}$  MAX phase in the Ti-rich and Al-rich layers,  $\text{TiO}_2$  and  $\text{Al}_2\text{O}_3$  are still the predominant phases. The SAED pattern for region 3 shows amorphous and nanocrystalline rings (Fig. 9j), and Fourier transform of

the white-marked area in Fig. 9i reveals an interplanar spacing of 0.33 nm, corresponding to the (110) plane of  $\text{SnO}_2$ .

To further verify the chemical composition of the passivation film, XPS analysis was conducted on the surfaces after potentiostatic polarization. In Fig. 10a, the Ti 2p spectrum shows binding energies of 459.2 eV [64] and 464.9 eV [65] for  $\text{Ti}_2(\text{Al, Sn})\text{C}$ , and 458.6 eV [66] and 464.3 eV [67] for  $\text{Ti}_2\text{AlC}$ , both of which correspond to  $\text{TiO}_2$ . The Al 2p spectrum (Fig. 10b) features a peak at 75.4 eV [68] for  $\text{Ti}_2(\text{Al, Sn})\text{C}$ , indicating the presence of  $\text{Al}_2\text{O}_3$ . The peak at 75.1 eV for the  $\text{Ti}_2\text{AlC}$  coating is related to a very small amount of Al, suggesting the presence of trace amounts of  $\text{Al}_2\text{O}_3$  on the surface. The Sn 3d spectrum (Fig. 10c) displays two peaks at binding energies of 487.1 eV [69] and 495.5 eV [70], corresponding to  $\text{SnO}_2$ . The C 1s spectrum shows peaks at binding energies of 285.3 eV and 287.2 eV for  $\text{Ti}_2(\text{Al, Sn})\text{C}$  and 285.2 eV for  $\text{Ti}_2\text{AlC}$ . These detected carbon components may relate to surface contaminants adsorbed during the sample preparation and the acetone/alcohol cleaning process. The XPS results indicate that the passivation film on the  $\text{Ti}_2(\text{Al, Sn})\text{C}$  coating contains three types of oxides:  $\text{TiO}_2$ ,  $\text{Al}_2\text{O}_3$ , and  $\text{SnO}_2$ .

Due to the corrosion in the coatings, metal ions can be released from the bipolar plates into the solution, thereby affecting the lifespan of PEMFCs. To confirm the dissolved metal ions after corrosion, we performed chemical composition analysis of the solution using ICP-OES after constant potential polarization. As shown in Table 4, the concentrations of Fe and Cr ions leached from SS316L are 0.448 mg/L and 0.318 mg/L for  $\text{Ti}_2\text{AlC}$ , and 0.077 mg/L and 0.064 mg/L for  $\text{Ti}_2(\text{Al, Sn})\text{C}$ . The concentrations of Fe and Cr ions in both coatings are below

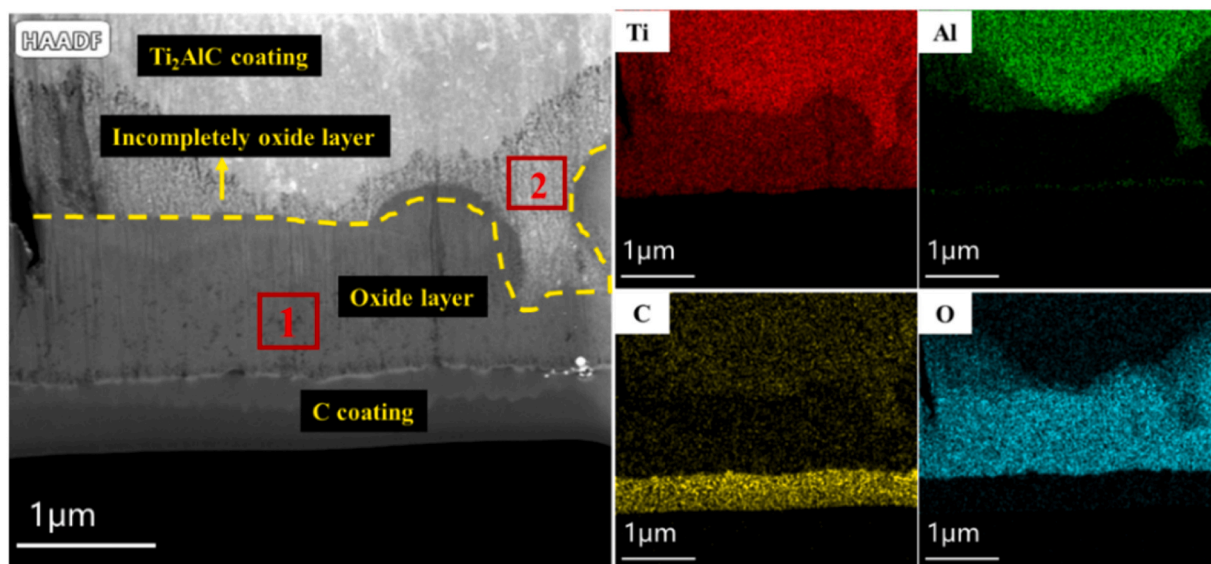


Fig. 7. STEM-HAADF image and EDS mapping of  $Ti_2AlC$  after potentiostatic polarization for 24 h in 0.5 mol  $H_2SO_4$  + 5 mg/L HF, 80 °C.

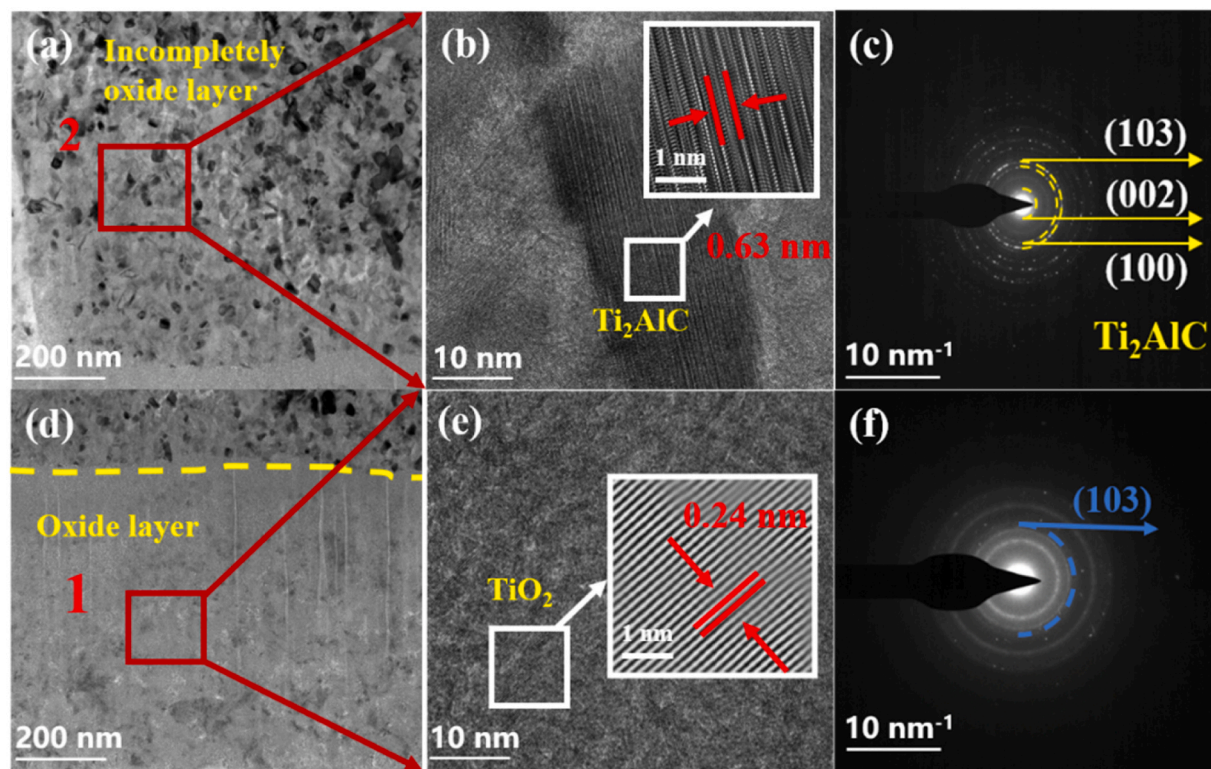


Fig. 8. (a, d) Bright-field image (b, e) HRTEM image, the inset is Fourier filtered images from (b, e) box. (c, f) The selected area electron diffraction (SAED) pattern.

10 mg/L and 5 mg/L, respectively[71]. This indicates that both coatings provide good protective effects for the bipolar plates.

### 3.4. Formation mechanism of the passive film

As is widely known, the formation of anodic passivation films occurs at the interface between the coating and the electrolyte. The migration of metallic elements is a key factor influencing the type of oxide present in the passivation film. Diffusion mediated by vacancies and its associated mechanisms provides an important theoretical foundation for understanding the dynamics of atomic diffusion in the MAX phase. When

the vibrational energies of atoms at the lattice nodes in a crystal reach a certain threshold, they can overcome the binding forces of surrounding atoms. This allows them to move from their original positions, creating vacancies. As the primary medium for atomic diffusion, the difficulty of vacancy formation is characterized by the vacancy formation energy ( $E_v$ ), which is the energy required for an atom to transition from the lattice to the crystal surface. For the  $Ti_2AlC$  and  $Ti_2(Al, Sn)C$  MAX phases, the vacancy formation energy can be calculated by the following equation[72]:

$$\Delta E_v = E_{defect} - E_{perfect} + \mu_i \tag{3-2}$$

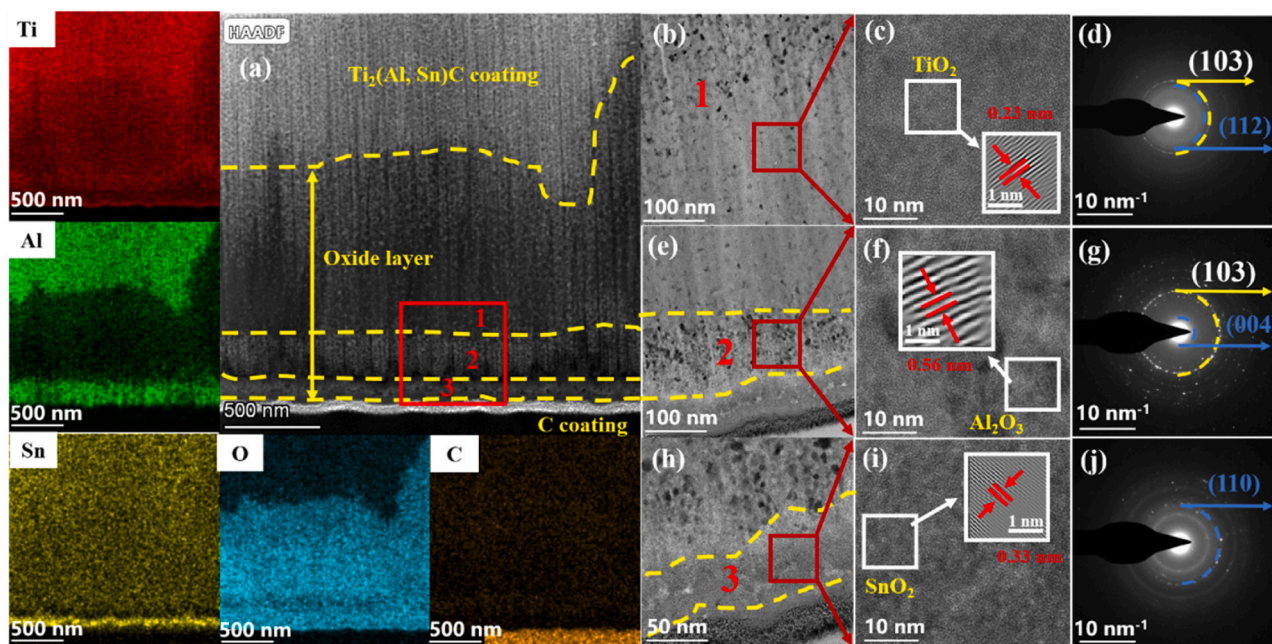


Fig. 9. (a) STEM-HAADF image and EDS mapping of  $\text{Ti}_2(\text{Al, Sn})\text{C}$  after potentiodynamic polarization for 24 h in 0.5 mol  $\text{H}_2\text{SO}_4 + 5 \text{ mg/L HF}$ , 80 °C: (b, e, h) Bright-field image. (c, f, i) HRTEM image. The inset is Fourier filtered images in (c, f, i). (d, g, j) The SAED pattern.

Table 3

The elemental content of the selected location in the STEM-HAADF image in Fig. 6(a).

Element content (at%)	Position 1	Position 2	Position 3
Ti	27.51	23.17	21.12
Al	5.92	23.38	1.92
Sn	2.54	1.88	6.35
C	7.80	8.32	5.85
O	56.23	43.25	64.76

Where the  $\Delta E_v$  represents the energy needed to form a vacancy in the system,  $E_{\text{defect}}$  is the total energy of  $\text{Ti}_2\text{AlC}$  or  $\text{Ti}_2(\text{Al, Sn})\text{C}$  supercell containing a single vacancy,  $E_{\text{perfect}}$  is the total energy of a supercell without any vacancies, and  $\mu_i$  denotes the chemical potential of the element. The chemical potential is closely linked to the crystal growth conditions. Therefore, the average atomic energy of the solid in its ground state is typically used as an approximation for the chemical potential. This approach allows for deriving an upper limit on the vacancy formation energy.

According to the aforementioned equation, the vacancy formation

energy of Ti and Al elements in  $\text{Ti}_2\text{AlC}$  and  $\text{Ti}_2(\text{Al, Sn})\text{C}$  were calculated, as illustrated in Fig. 11 a-b. For the  $\text{Ti}_2\text{AlC}$  crystal structure, the formation energies of Ti and Al vacancies are 5.619 eV and 2.796 eV respectively. Similarly, in the  $\text{Ti}_2(\text{Al, Sn})\text{C}$  system, the vacancy formation energies are 5.285 eV for Ti and 2.993 eV for Al. Consequently, it can be inferred that the solid solution of Sn atoms in  $\text{Ti}_2\text{AlC}$  significantly reduces the vacancy energy of Ti. This implies that the addition of Sn elements lowers the formation energy, which favors the high mobility of Ti atoms and promotes the generation of  $\text{TiO}_2$ . While, the change in the formation energy of Al vacancies is not particularly evident. It is worth mentioning that regardless of the presence of Sn solid solution atoms, the Al vacancy remains the most energetically favorable single atomic

Table 4

Chemical composition of aqueous solutions determined by ICP-OES after electrochemical corrosion tests.

Samples	Ti (mg/L)	Al (mg/L)	Fe (mg/L)	Cr (mg/L)
$\text{Ti}_2\text{AlC}$	1.600	3.160	0.448	0.077
$\text{Ti}_2(\text{Al, Sn})\text{C}$	1.710	1.900	0.318	0.064

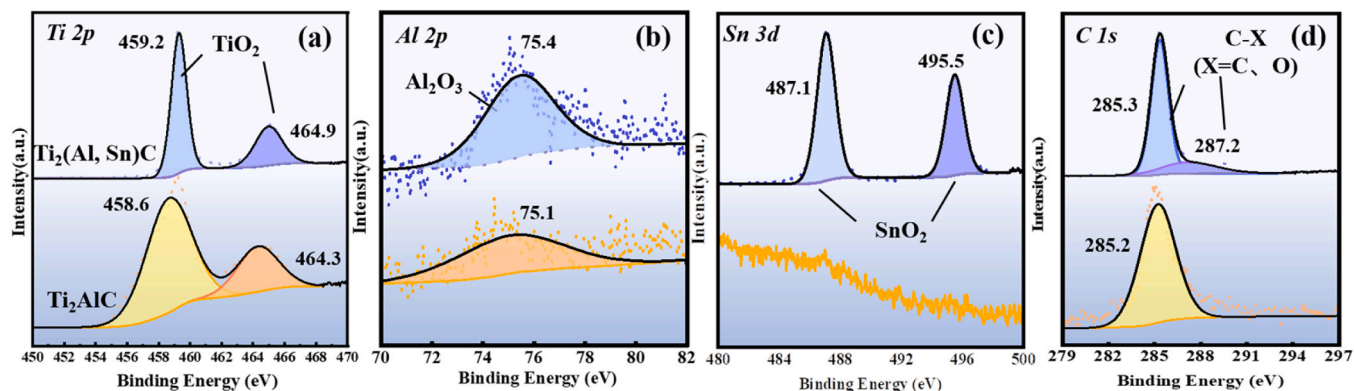


Fig. 10. XPS spectra of (a) Ti 2p, (b) Al 2p, (c) Sn 3d and (d) C 1s for the  $\text{Ti}_2\text{AlC}$  and  $\text{Ti}_2(\text{Al, Sn})\text{C}$  coatings after potentiostatic polarization for 24 h in 0.5 mol  $\text{H}_2\text{SO}_4 + 5 \text{ mg/L HF}$ , 80 °C.

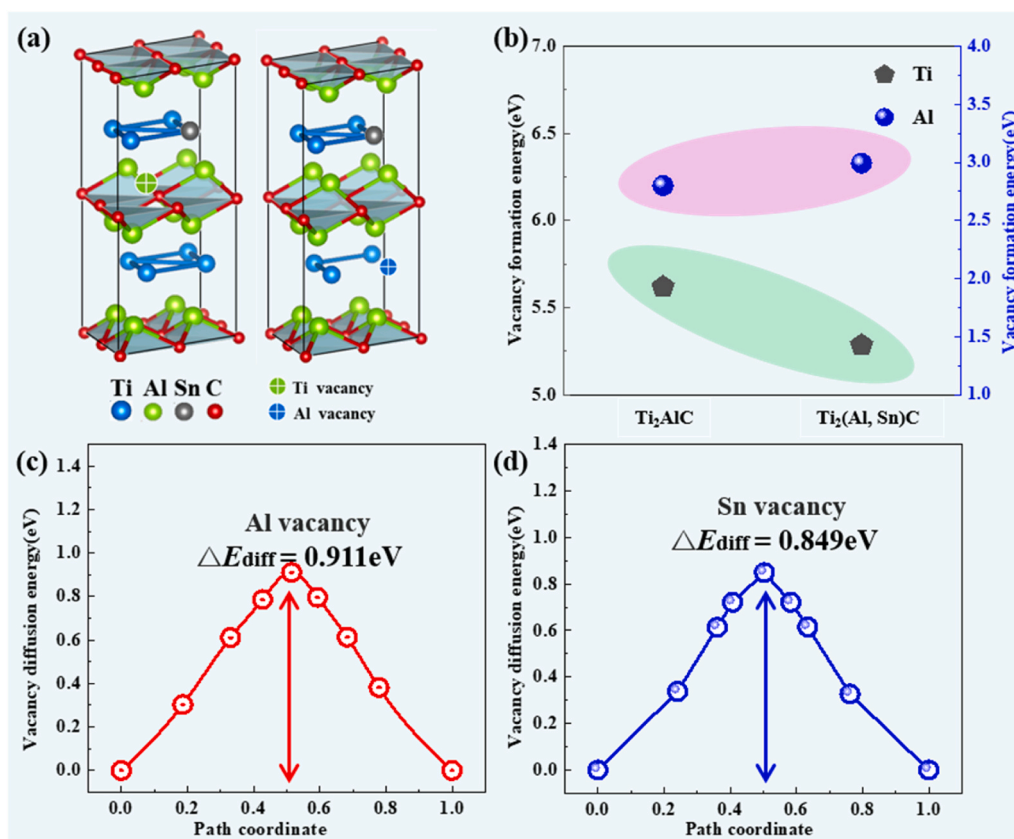


Fig. 11. (a) Vacancies model diagram of Ti and Al atoms in Ti<sub>2</sub>(Al, Sn)C coating. (b) Vacancy formation energies of Ti and Al atoms in Ti<sub>2</sub>AlC and Ti<sub>2</sub>(Al, Sn)C coating. Diffusion activation energy of Al and Sn atoms in Ti<sub>2</sub>(Al, Sn)C coating:(c) Al, (d) Sn.

vacancy.

To assess the diffusion behavior of atomic motion within the coatings, it is essential to consider both the vacancy formation energy and the diffusion barrier. Therefore, we further simulated the atomic migration energy here. This comprehensive assessment involves analyzing the diffusion paths of neighboring vacancies along the basal plane. The migration energies of Al and Sn atoms in Ti<sub>2</sub>(Al, Sn)C were calculated by identifying the transition states at both ends of the defect model. The simulated diffusion paths for Al and Sn atoms, along with the calculated diffusion energy curves for each atom in the lattice, are illustrated in Fig. 11c-d. It is worth mentioning that in our previous study[17], the migration energies of various atoms in Ti<sub>2</sub>AlC have been calculated. The results showed that the migration energies of Ti Al C were 2.297 eV, 0.901 eV, and 3.104 eV, respectively, which implies that Al is easier to migrate. Here the migration energies of Al and Sn atoms in Ti<sub>2</sub>(Al, Sn)C solid solution are further calculated in comparison. The findings reveal that the migration energies for Al and Sn in Ti<sub>2</sub>(Al, Sn)C are 0.911 eV and 0.849 eV, respectively. Hence, the diffusion barrier of Sn atoms in Ti<sub>2</sub>(Al, Sn)C is lower than that of Al atoms. This implies that a reaction may occur between Sn atoms and exposed oxygen, leading to the formation of SnO<sub>2</sub> passivation film on the surface of the coating. This further elucidates the phenomenon of the SnO<sub>2</sub> film formation on the surface of the Ti<sub>2</sub>(Al, Sn)C coating after electrochemical testing.

Therefore, the presence of low vacancy formation energy and low diffusion energy for Al atoms contributes to enhanced migration rates of Al atoms. This leads to the preferential outward diffusion of Al atoms to capture oxygen and form Al<sub>2</sub>O<sub>3</sub>. This elucidates the formation of Al<sub>2</sub>O<sub>3</sub> passivation film on the surfaces of both Ti<sub>2</sub>AlC and Ti<sub>2</sub>(Al, Sn)C coatings during the polarization process. However, for the Ti<sub>2</sub>AlC coating, in the corrosive solution of HF, F<sup>-</sup> ions can disrupt Al<sub>2</sub>O<sub>3</sub>. This disruption leads to its ongoing dissolution[73,74], resulting in some Al ions dissolving into the solution (as shown in Table 4). Consequently, there is less Al<sub>2</sub>O<sub>3</sub>

and more TiO<sub>2</sub> on the surface of coating. Interestingly, for the Ti<sub>2</sub>(Al, Sn)C coating, Sn preferentially oxidizes to form a SnO<sub>2</sub> layer. The phenomenon inhibits the penetration of corrosive media, effectively preventing the degradation of the passive Al<sub>2</sub>O<sub>3</sub> layer. It also enhances the density and protective performance of the subsequently formed Al<sub>2</sub>O<sub>3</sub> layer. Additionally, the Al<sub>2</sub>O<sub>3</sub> layer, generated from the oxidation of Al, offers better barrier properties and protection than the TiO<sub>2</sub> layer. The layered oxide film structure maximizes the individual advantages of each oxide layer, thereby improving the corrosion resistance of the coating. The schematic diagram showing the passivation mechanism and process of Ti<sub>2</sub>AlC and Ti<sub>2</sub>(Al, Sn)C coating is detailed shown in Fig. 12.

#### 4. Conclusion

In summary, we successfully prepared Ti<sub>2</sub>AlC and Ti<sub>2</sub>(Al, Sn)C coatings using HiPIMS/DCMS combined with subsequent annealing treatment. A series of comprehensive experiments were conducted to compare the two coatings in terms of electrochemical performance, passivation film evolution and conductivity. Under harsh acidic solution, the layered oxide structure formed on the surface of the Ti<sub>2</sub>(Al, Sn)C coating consists of TiO<sub>2</sub>, Al<sub>2</sub>O<sub>3</sub>, and SnO<sub>2</sub> layers. The SnO<sub>2</sub> layer effectively prevents the penetration of corrosive media, protecting the Al<sub>2</sub>O<sub>3</sub> layer from degradation while enhancing its density and protective effect. At the same time, the layered oxide structures can take advantages of the properties of each oxide film, significantly improving the corrosion resistance of the coating surface. Consequently, compared to the Ti<sub>2</sub>AlC coating, the Ti<sub>2</sub>(Al, Sn)C coating exhibits the lowest corrosion current density ( $9.62 \times 10^{-7}$  A/cm<sup>2</sup>). Additionally, the good conductivity of the SnO<sub>2</sub> layer stabilizes the electrical performance of the Ti<sub>2</sub>(Al, Sn)C coating after corrosion. This research not only deepens the understanding of the conductivity and corrosion mechanisms of metal bipolar

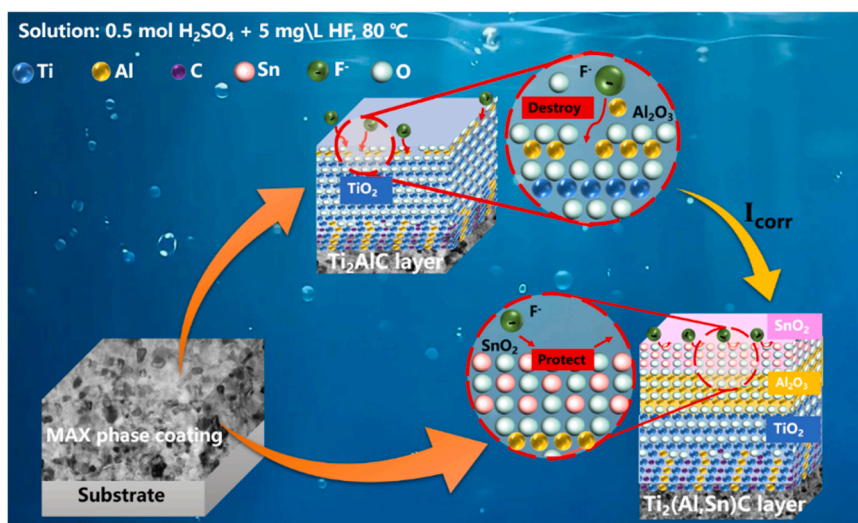


Fig. 12. Schematic diagram showing the passivation mechanism and process of  $\text{Ti}_2\text{AlC}$  and  $\text{Ti}_2(\text{Al, Sn})\text{C}$  coating in  $0.5 \text{ mol H}_2\text{SO}_4 + 5 \text{ mg/L HF}$ ,  $80^\circ\text{C}$ .

plate MAX phase coatings, but also aids in the design and development of high-performance, long-lasting PEMFCs metal plate materials. In addressing the challenges of commercial application, fuel cell bipolar plates face issues such as high production costs, corrosion susceptibility, and the need for reliable electrical conductivity. Our coatings provide significant benefits by enhancing corrosion resistance, improving conductivity. Additionally, this work lays a theoretical and technical foundation for scalable production, which is crucial for the widespread adoption of fuel cells in applications. By overcoming these challenges, our coatings can contribute to the commercial viability and long-term success of fuel cell technologies.

#### CRediT authorship contribution statement

**Jiayue Zhang:** Writing – original draft, Investigation, Data curation. **Yan Zhang:** Visualization, Software, Investigation. **Zhenyu Wang:** Supervision, Funding acquisition. **Guanshui Ma:** Writing – review & editing, Supervision, Funding acquisition. **Anfeng Zhang:** Methodology. **Kwang-Ryeol Lee:** Supervision. **Aiying Wang:** Writing – review & editing, Supervision, Funding acquisition, Conceptualization.

#### Declaration of Competing Interest

The authors declare that they have no known competing financial interests or personal relationships that could have appeared to influence the work reported in this paper.

#### Acknowledgments

Jiayue Zhang and Yan Zhang contributed equally to this work. This work was financially supported by the National Science Found for Distinguished Young Scholars of China (No. 52025014), the National Natural Science Foundation of China (52171090), the Zhejiang Provincial Natural Science Foundation of China (No. LD24E010003) and the Natural Science Foundation of Ningbo (No.2023J410 and 2023QL049).

#### Data availability

Data will be made available on request.

#### References

- [1] A.G. Olabi, T. Wilberforce, M.A. Abdelkareem, Fuel cell application in the automotive industry and future perspective, *Energy* 214 (2020) 118955.
- [2] Y. Fu, G.Q. Lin, M. Hou, B. Wu, Z.G. Shao, B.L. Yi, Carbon-based films coated 316L stainless steel as bipolar plate for proton exchange membrane fuel cells, *Int. J. Hydrog. Energy* 34 (2009) 405–409.
- [3] J.L. Lv, T.X. Liang, C. Wang, Comparison of corrosion behavior between coarse grained and nanocrystalline Ni-Fe alloys in chloride solutions and proton exchange membrane fuel cell environment by EIS, XPS and Raman spectra techniques, *Energy* 112 (2016) 67–74.
- [4] J.D. Majumdar, I. Manna, *Laser processing of materials*, *Sadhana* 28 (2003) 495–562.
- [5] J.D. Majumdar, I. Manna, *Laser material processing*, *Int. Mater. Rev.* 56 (2011) 341–388.
- [6] S. Anishetty, T. Bera, S.K. Karak, J.D. Majumdar, I. Manna, Microstructure and properties of laser surface melted AISI 316L stainless steel, *J. Mater. Eng. Perform.* (2024) 1–16.
- [7] T. Bera, I. Manna, J.D. Majumdar, Titanium carbide (TiC) dispersed surface on titanium based alloy (Ti-13Nb-13Zr) by in-situ laser composite surfacing and its wear performance, *J. Mater. Sci.* 328 (2024) 118394.
- [8] Y. Wang, D.O. Northwood, An investigation into the effects of a nano-thick gold interlayer on polypyrrole coatings on 316L stainless steel for the bipolar plates of PEPA fuel cells, *J. Power Sources* 175 (2008) 40–48.
- [9] B. Chen, W. Ke, M.J. Luo, J. Wang, Z.K. Tu, M. Pan, H.N. Zhang, X.W. Liu, W. Liu, Operation characteristics and carbon corrosion of PEMFC (Proton exchange membrane fuel cell) with dead-ended anode for high hydrogen utilization, *Energy* 91 (2015) 799–806.
- [10] H. Husby, O.A. Kongstein, A. Oedegaard, F. Seland, Carbon-polymer composite coatings for PEM fuel cell bipolar plates, *Int. J. Hydrog. Energy* 39 (2014) 951–957.
- [11] H. Li, P. Guo, D. Zhang, L.L. Liu, Z.Y. Wang, G.S. Ma, Y. Xin, P.L. Ke, H. Saito, A. Y. Wang, Interface-induced degradation of amorphous carbon films/stainless steel bipolar plates in proton exchange membrane fuel cells, *J. Power Sources* 469 (2020) 228269.
- [12] Z. Zhang, X.M. Duan, D.C. Jia, Y. Zhou, S. van der Zwaag, On the formation mechanisms and properties of MAX phases: a review, *J. Eur. Ceram. Soc.* 41 (2021) 3851–3878.
- [13] C.Z. Wu, X.L. Wu, J.X. Ding, K.K. Ding, P.G. Zhang, C.J. Ma, D.M. Hu, D.M. Liu, S. H. Zhang, W. Zheng, L. Pan, Z.M. Sun, Achieving highly conductive  $\text{Ag}/\text{Ti}_3\text{AlC}_2$  composite by inhibiting interdiffusion, *Scr. Mater.* 255 (2025), 116343–116343.
- [14] X.L. Wu, C.Z. Wu, X.P. Wei, W.J. Sun, C.J. Ma, Y.D. Zhang, G.G. Li, L.M. Chen, D. D. Wang, P.G. Zhang, Z.M. Sun, J.X. Ding, Influence of nano-mechanical evolution of  $\text{Ti}_3\text{AlC}_2$  ceramic on the arc erosion resistance of Ag-based composite electrical contact material, *J. Adv. Ceram.* 13 (2024) 176–188.
- [15] X.J. Duan, Z. Fang, T. Yang, C.Y. Guo, Z.K. Han, D. Sarker, X.M. Hou, E.H. Wang, Maximizing the mechanical performance of  $\text{Ti}_3\text{AlC}_2$ -based MAX phases with aid of machine learning, *J. Adv. Ceram.* 11 (2022) 1307–1318.
- [16] G.S. Ma, H.C. Wu, Z. Fang, X.H. Zhou, R.D. Chen, W. Yang, J.Y. Zhang, Z.Y. Wang, A.Y. Wang, Phase formation mechanism of  $\text{Cr}_2\text{AlC}$  MAX phase coating: in-situ TEM characterization and atomic-scale calculations, *J. Mater. Sci. Technol.* 206 (2025) 176–184.
- [17] Z.C. Li, Y. Zhang, K.H. Wang, Z.Y. Wang, G.S. Ma, P.L. Ke, A.Y. Wang, Highly dense passivation enhanced corrosion resistance of  $\text{Ti}_2\text{AlC}$  MAX phase coating in 3.5 wt% NaCl solution, *Corros. Sci.* 228 (2024) 111820.

- [18] G.X. Zhou, Z.C. Li, J.H. Yuan, R.D. Chen, Z.Y. Wang, P.L. Ke, A.Y. Wang, Enhanced crystalline growth of Cr<sub>2</sub>AlC MAX phase coating by hybrid DCMS/HIPIMS at low temperature, *Appl. Surf. Sci.* 666 (2024) 160371.
- [19] Z.M. Sun, Progress in research and development on MAX phases: a family of layered ternary compounds, *Int. Mater. Rev.* 56 (2011) 143–166.
- [20] Z.C. Li, Z.Y. Wang, G.S. Ma, R.D. Chen, W. Yang, K.H. Wang, P.L. Ke, A.Y. Wang, High-performance Cr<sub>2</sub>AlC MAX phase coatings for ATF application: interface design and oxidation mechanism, *Corros. Commun.* 13 (2024) 27–36.
- [21] G.Y. Liu, F.G. Hou, S.L. Peng, X.D. Wang, B.Z. Fang, Process and challenges of stainless steel based bipolar plates for proton exchange membrane fuel cells, *Int. J. Miner. Metall. Mater.* 29 (2022) 1099–1119.
- [22] R.A. Antunes, M.C.L. de Oliveira, G. Ett, V. Ett, Carbon materials in composite bipolar plates for polymer electrolyte membrane fuel cells: a review of the main challenges to improve electrical performance, *J. Power Sources* 196 (2011) 2945–2961.
- [23] Z. Ming, R. Wang, C. Chen, H.B. Zhang, G.J. Zhang, Electrochemical study on the corrosion behavior of Ti<sub>3</sub>SiC<sub>2</sub> in 3.5% NaCl solution, *RSC Adv.* 7 (2017) 12534–12540.
- [24] D. Li, Y. Liang, X.X. Liu, Y.C. Zhou, Corrosion behavior of Ti<sub>3</sub>AlC<sub>2</sub> in NaOH and H<sub>2</sub>SO<sub>4</sub>, *J. Eur. Ceram. Soc.* 30 (2010) 3227–3234.
- [25] J.L. Lu, N. Abbas, J.N. Tang, J. Tang, G.M. Zhu, Synthesis and characterization of conductive ceramic MAX-phase coatings for metal bipolar plates in simulated PEMFC environments, *Corros. Sci.* 158 (2019) 108106.
- [26] G.S. Ma, D. Zhang, P. Guo, H. Li, Y. Xin, Z.Y. Wang, A.Y. Wang, Phase orientation improved the corrosion resistance and conductivity of Cr<sub>2</sub>AlC coatings for metal bipolar plates, *J. Mater. Sci. Technol.* 105 (2022) 36–44.
- [27] G.S. Ma, J.H. Yuan, R.D. Chen, H. Li, H.C. Wu, J.S. Yan, Z.Y. Wang, A.Y. Wang, Balancing the corrosion resistance and conductivity of Cr-Al-C coatings via annealing treatment for metal bipolar plates, *Appl. Surf. Sci.* 597 (2022) 153670.
- [28] Y. Zhang, A.F. Zhang, Z.C. Li, Z.Y. Wang, P.L. Ke, A.Y. Wang, Electrochemical corrosion inhibition of Cr<sub>2</sub>AlC MAX phase coatings via Mo solid solution: Comprehensive experimental and simulation study, *J. Phys. Chem. C* 128 (2024) 3916–3923.
- [29] K.H. Wang, Z.C. Li, Y. Zhang, G.S. Ma, G.X. Zhou, P.L. Ke, Z.Y. Wang, A.Y. Wang, Solid solution of zirconium on the M-site strengthening Ti<sub>2</sub>AlC MAX phase coatings, *Surf. Interfaces* 51 (2024) 104678.
- [30] A.F. Zhang, K.H. Wang, Y. Zhang, G.S. Ma, W. Yang, G.X. Zhou, P.L. Ke, Z.Y. Wang, A.Y. Wang, Towards developing Ti<sub>2</sub>AlC coatings with improved oxidation resistance via Nb solid solution, *J. Alloy. Compd.* 1002 (2024) 175524.
- [31] V.D. Jovic, B.M. Jovic, S. Gupta, T. El-Raghy, M.W. Barsoum, Corrosion behavior of select MAX phases in NaOH, HCl and H<sub>2</sub>SO<sub>4</sub>, *Corros. Sci.* 48 (2006) 4274–4282.
- [32] Y.W. Cao, C.S. Guo, D.T. Wu, Y. Zou, Synthesis and corrosion resistance of solid solution Ti<sub>3</sub>(Al<sub>1-x</sub>Si<sub>x</sub>)C<sub>2</sub>, *J. Alloy. Compd.* 867 (2021) 159126.
- [33] G.P. Bei, B.J. Pedimonte, T. Fey, P. Greil, Oxidation behavior of MAX phase Ti<sub>2</sub>Al<sub>(1-x)Sn<sub>x</sub></sub>C solid solution, *J. Am. Ceram. Soc.* 96 (2013) 1359–1362.
- [34] G.Q. Wang, Effect of calcination temperature on surface crystallization and conductivity of ATO/TiO<sub>2</sub> powder, *J. Wuhan. Inst. Technol.* 33 (2011) 30–33.
- [35] C.Y. Guo, X.J. Duan, Z. Fang, Y.S. Zhao, T. Yang, E.H. Wang, X.M. Hou, A new strategy for long-term complex oxidation of MAX phases: database generation and oxidation kinetic model establishment with aid of machine learning, *Acta Mater.* 241 (2022) 118378.
- [36] X.J. Duan, Z. Fang, C.Y. Guo, Z.K. Han, X.M. Hou, E.H. Wang, Maximizing the mechanical performance of Ti<sub>3</sub>AlC<sub>2</sub> based MAX phases with aid of machine learning, *J. Adv. Ceram.* 11 (2022) 1307–1318.
- [37] C.Y. Guo, E.H. Wang, Y.S. Liu, Y.P. Zheng, T. Yang, X.M. Hou, Effect of Sn doping concentration on the oxidation process of Al-containing MAX phase (Ti<sub>3</sub>AlC<sub>2</sub>) combining simulation with experiment, *Fundam. Res.* 2 (2022) 114–122.
- [38] C.Y. Guo, E.H. Wang, S.Z. Wang, X.M. Hou, Z.J. He, T.X. Liang, K.C. Chou, Oxidation mechanism of MAX phases (Ti<sub>3</sub>AlC<sub>2</sub> powders) with and without Sn doping, *Corros. Sci.* 180 (2021) 109197.
- [39] M.D. Segall, P.J.D. Lindan, M.J. Probert, C.J. Pickard, P.J. Hasnip, S.J. Clark, M. C. Payne, First-principles simulation: ideas, illustrations and the CASTEP code, *J. Phys. Condens. Matter* 14 (2002) 2717–2744.
- [40] J.P. Perdew, K. Burke, M. Ernzerhof, Generalized gradient approximation made simple, *Phys. Rev. Lett.* 77 (1996) 3865–3868.
- [41] M.A. Ali, S.H. Naqib, Recently synthesized (Ti<sub>1-x</sub>Mo<sub>x</sub>)<sub>2</sub>AlC (0 ≤ x ≤ 0.20) solid solutions: deciphering the structural, electronic, mechanical and thermodynamic properties via ab initio simulations, *RSC Adv.* 10 (2020) 31535–31546.
- [42] N. Govind, M. Petersen, G. Fitzgerald, D. King-Smith, J. Andzelm, A generalized synchronous transit method for transition state location, *Comput. Mater. Sci.* 28 (2003) 250–258.
- [43] Z.Y. Wang, J. Sun, B.B. Xu, Y.R. Liu, P.L. Ke, A.Y. Wang, Reducing the self-healing temperature of Ti<sub>2</sub>AlC MAX phase coating by substituting Al with Sn, *J. Eur. Ceram. Soc.* 40 (2020) 197–201.
- [44] H.J. Lee, S.Y. Kim, Y.I. Lee, J. Byun, Synthesis and reaction path of Ti-Al-C MAX phases by reaction with Ti-Al intermetallic compounds and TiC, *J. Am. Ceram. Soc.* 106 (2023) 7230–7239.
- [45] Z. Mahmoudi, S.H. Tabaian, H.R. Rezaie, F. Mahboubi, M.J. Ghazali, Synthesis of Ti<sub>2</sub>AlC & Ti<sub>3</sub>AlC<sub>2</sub> MAX phases by Arc-PVD using Ti-Al target in C<sub>2</sub>H<sub>2</sub>/Ar gas mixture and subsequent annealing, *Ceramics* 46 (2020) 4968–4975.
- [46] W.C. Peng, Y.C. Chen, J.L. He, S.L. Ou, R.H. Horng, D.S. Wu, Tunability of p-and n-channel TiO<sub>x</sub> thin film transistors, *Chem. Mater.* 26 (2014) 2372–2381.
- [47] O. Wilhelmsson, J.-P. Palmquist, E. Lewin, J. Emmerlich, P. Eklund, P.Å. Persson, H. Högberg, S. Li, R. Ahuja, O. Eriksson, Deposition and characterization of ternary thin films within the Ti–Al–C system by DC magnetron sputtering, *J. Cryst. Growth* 291 (2006) 290–300.
- [48] M. Magnuson, O. Wilhelmsson, J.-P. Palmquist, U. Jansson, M. Mattesini, S. Li, R. Ahuja, O. Eriksson, Electronic structure and chemical bonding in Ti<sub>2</sub>AlC investigated by soft x-ray emission spectroscopy, *Phys. Rev. B* 74 (2006) 195108.
- [49] H. Yin, X.D. He, K.B. Qin, G.P. Song, Y.T. Zheng, Y.L. Bai, Long-term oxidation of Ti<sub>3</sub>Al<sub>0.8</sub>Sn<sub>0.2</sub>C<sub>2</sub> in air at 1200 °C, *Open Ceram.* 18 (2024) 100605.
- [50] R.I. Hegde, S.R. Sainkar, S. Badrinarayanan, A.P.B. Sinha, A study of dilute tin alloys by x-ray photoelectron spectroscopy, *J. Electron Spectrosc. Relat. Phenom.* 24 (1981) 19–25.
- [51] Youichi Ohno, Electronic structure of the misfit-layer compounds PbTiS<sub>3</sub> and SnNb<sub>3</sub>, *Phys. Rev. B* 44 (1991) 1281–1291.
- [52] X.P. Cao, L.L. Cao, W.Q. Yao, X.Y. Ye, Structural characterization of Pd-doped SnO<sub>2</sub> thin films using XPS, *Surf. Interface Anal.* 24 (1996) 662–666.
- [53] J. Halim, M.R. Lukatskaya, K.M. Cook, J. Lu, C.R. Smith, L.-Å. Näslund, S.J. May, L. Hultman, Y. Gogotsi, P. Eklund, Transparent conductive two-dimensional titanium carbide epitaxial thin films, *Chem. Mater.* 26 (2014) 2374–2381.
- [54] L. Yuan, H.M. Wang, Corrosion behaviors of a γ-toughened Cr<sub>13</sub>Ni<sub>5</sub>Si<sub>2</sub>/Cr<sub>3</sub>Ni<sub>5</sub>Si<sub>2</sub> multi-phase ternary metal silicide alloy in NaCl solution, *Electrochim. Acta* 54 (2008) 421–429.
- [55] A.M.M. dos Santos, R.J.C. Batista, L.A.M. Martins, M. Ilha, M.Q. Vieira, D. R. Miquita, F.C.R. Guma, I.L. Mueller, T.M. Manhabosco, Corrosion and cell viability studies of graphite-like hydrogenated amorphous carbon films deposited on bare and nitrified titanium alloy, *Corros. Sci.* 82 (2014) 297–303.
- [56] T. Ge, L. Chen, P.F. Gu, X.D. Ren, X.M. Chen, Microstructure and corrosion resistance of TiC/Inconel 625 composite coatings by extreme high speed laser cladding, *Opt. Laser Technol.* 150 (2022) 107919.
- [57] J. Pan, D. Thierry, C. Leygraf, Electrochemical impedance spectroscopy study of the passive oxide film on titanium for implant application, *Electrochim. Acta* 41 (1996) 1143–1153.
- [58] M.M. Thaddeus, A review of electrochemical corrosion fundamentals, *Ind. Eng. Chem., Prod. Res. Dev.* 17 (1978) 93–184.
- [59] B.R. Barat, E. Cano, In situ electrochemical impedance spectroscopy measurements and their interpretation for the diagnostic of metallic cultural heritage: a review, *ChemElectroChem* 5 (2018) 2698–2716.
- [60] H.H. Strehblow, Combined surface analytical and electrochemical studies for corrosion research, *Surf. Interface Anal.* 12 (1988) 363–379.
- [61] D. Chidambaram, C.R. Clayton, M.R. Dorfman, Evaluation of the electrochemical behavior of HVOF-sprayed alloy coatings, *Surf. Coat. Technol.* 176 (2004) 307–317.
- [62] X.H. Deng, Y.H. Zhao, Study on fatigue life of aero engine compressor blades, *J. Xinjiang Inst. Technol.* (2000) 221–225.
- [63] B.B. Chen, F.Y. Chang, J. Yang, H. Tang, C.S. Li, Microstructure and phase transformation of Ti<sub>3</sub>AlC<sub>2</sub> (A = Al, Si) in hydrofluoric acid solution, *Cryst. Res. Technol.* 49 (2014) 813–819.
- [64] M. Murata, K. Wakino, S. Ikeda, X-ray photoelectron spectroscopic study of perovskite titanates and related compounds: an example of the effect of polarization on chemical shifts, *J. Electron Spectrosc.* 6 (1975) 459–464.
- [65] S.O. Saied, J.L. Sullivan, T. Choudhury, C.G. Pearce, A comparison of ion and fast atom beam reduction in TiO<sub>2</sub>, *Vacuum* 38 (1988) 917–922.
- [66] T. Hanawa, M. Ota, Calcium phosphate naturally formed on titanium in electrolyte solution, *Biomaterials* 12 (1991) 767–774.
- [67] J.L. Ong, L.C. Lucas, G.N. Raikar, J.C. Gregory, Electrochemical corrosion analyses and characterization of surface-modified titanium, *Appl. Surf. Sci.* 72 (1993) 7–13.
- [68] I. Olefjord, H.J. Mathieu, P. Marcus, Intercomparison of surface analysis of thin aluminium oxide films, *Surf. Interface Anal.* 15 (1990) 681–692.
- [69] S. Badrinarayanan, A.B. Mandale, V.G. Gunjkar, A.P.B. Sinha, Mechanism of high-temperature oxidation of tin selenide, *J. Mater. Sci.* 21 (1986) 3333–3338.
- [70] W.K. Choi, H.J. Jung, S.K. Koh, Chemical shifts and optical properties of tin oxide films grown by a reactive ion assisted deposition, *J. Vac. Sci. Technol. A* 14 (1998) 359.
- [71] M. Xie, Z.S. Chao, Research progress of Fe/N/C oxygen reduction reaction catalyst for fuel cell in past decade, *Mater. Sci.* 10 (2020) 766–785.
- [72] J. Wang, Y. Zhou, T. Liao, J. Zhang, Z. Lin, A first-principles investigation of the phase stability of Ti<sub>2</sub>AlC with Al vacancies, *Scr. Mater.* 58 (2008) 227–230.
- [73] A.M. Lucente, J.R. Scully, Pitting and alkaline dissolution of an amorphous–nanocrystalline alloy with solute-lean nanocrystals, *Corros. Sci.* 49 (2007) 2351–2361.
- [74] M. Cao, L. Liu, Z. Yu, L. Fan, Y. Li, F. Wang, Electrochemical corrosion behavior of 2A02 Al alloy under an accelerated simulation marine atmospheric environment, *J. Mater. Sci. Technol.* 35 (2019) 651–659.